ELSEVIER

Contents lists available at ScienceDirect

## **Journal of Pharmaceutical Sciences**

journal homepage: www.jpharmsci.org



Pharmaceutics, Drug Delivery and Pharmaceutical Technology

# Advanced Chemical and Imaging Methods for Studying Structure Morphology and Excipients Solid State Transformations in Pharmaceutical Multiparticulate Formulations



Elizabeth J. Legge<sup>a</sup>, Mark Stewart<sup>a</sup>, Lourdes P. Contreras Chávez<sup>b</sup>, Hannah Zhang<sup>a</sup>, Dimitrios Tsikritsis<sup>a</sup>, Natalie A. Belsey<sup>a,c</sup>, Mark McAllister<sup>b</sup>, John Richard Murphy<sup>b</sup>, Ken Mingard<sup>a</sup>, Caterina Minelli<sup>a,\*</sup>

- <sup>a</sup> National Physical Laboratory, Teddington, TW11 0LW, UK
- <sup>b</sup> Worldwide Research and Development and Medical, Drug Product Design, Pfizer Ltd., Ramsgate Road, Sandwich, CT13 9NJ, UK
- <sup>c</sup> School of Chemistry and Chemical Engineering, University of Surrey, Guildford, GU2 7XH, UK

#### ARTICLE INFO

#### Article history: Received 17 January 2024 Revised 7 May 2024 Accepted 7 May 2024 Available online 20 May 2024

Keywords:
Multiparticulates
Physicochemical properties
Stability
Imaging methods
Formulation
Poloxamer 407
Glyceryl Dibehenate
Stimulated Raman scattering microscopy
Environmental scanning electron microscopy

#### ABSTRACT

The formulation of paediatric medicines faces significant challenges to meet the requirements for safe and accurate administration, while maintaining a suitable taste. Multiparticulate formulations have a strong potential to address these challenges because they combine dose flexibility with ease of administration. Understanding the stability of multiparticulate formulations over storage as a function of time and environmental parameters, such as humidity and temperature, is important to manage their commercialisation and use. In this work, we have expanded the toolkit of available techniques for studying multiparticulates beyond those such as scanning electron microscopy (SEM) and confocal laser scanning microscopy. We include advanced methods of environmentally-controlled SEM to monitor temperature- and humidity-induced changes *in-situ*, and a variety of Raman spectroscopies including stimulated Raman scattering microscopy to identify and localise the different ingredients at the surface and inside the multiparticulates. These techniques allowed unprecedented monitoring of specific changes to the particulate structure and distribution of individual ingredients due to product aging. These methods should be considered as valuable novel tools for in-depth characterisation of multiparticulate formulations to further understand chemical changes occurring during their development, manufacturing and long-term storage. We envisage these techniques to be useful in furthering the development of future medicine formulations.

© 2024 The Authors. Published by Elsevier Inc. on behalf of American Pharmacists Association. This is an open access article under the CC BY-NC-ND license (http://creativecommons.org/licenses/by-nc-nd/4.0/)

### Introduction

Multiparticulate (MP) formulations show significant potential for delivering viable paediatric medicines thanks to the flexibility they offer in terms of dosage and administration. The excipient types and properties are selected to optimise shelf life and active pharmaceutical ingredient (API) release after administering. The choice of excipients and relative concentrations allow control over the release rate. However, environmental conditions such as humidity and temperature can induce changes to the MP structure and chemistry over time. This in turn can impact the release behaviour, therapeutic index and efficacy of a medicine. To map out mitigation strategies during manufacturing, distribution and administration of these

medicines, it is important to understand how environmental conditions affect formulations during aging.

Understanding MP stability requires the analysis of their physical and chemical attributes before, during and after storage. Subjecting pharmaceutical materials to conditions of either elevated humidity, temperature, or both has long been accepted as a method for accelerating their chemical degradation. In this study we use the same principles to study the changes of MP systems under conditions which simulate an accelerated aging process.

MPs are particle systems generally capable of delivering therapeutics with a satisfactory sustained release or controlled release profile. MPs produced by melt-spray-congealing (MSC) technology, are close-to-spherical particles that range from 10  $\mu$ m to 500  $\mu$ m in size. MSC microspheres are formed by suspending solid API in a molten carrier matrix, which is then fed onto a spinning-disk atomizer in order to form droplets, and finally, allowing the droplets to congeal into

<sup>\*</sup> Corresponding author.

E-mail address: caterina.minelli@npl.co.uk (C. Minelli).

microspheres upon cooling.<sup>10,11</sup> The active ingredients are ideally homogenously distributed in a polymeric network within the particles. A wide variety of low melting point materials have been used to form the molten carrier matrix, such as: waxes, fatty acids, glycerides, polyglycol esters of fatty acids, stearic acid, stearyl alcohol, and other materials that are solid at room temperature and melt without decomposition within the standard operating temperature of the MSC equipment, typically 80°C to 90°C.<sup>12</sup>

The aim of the present study is to develop and apply advanced chemical and imaging methods to investigate the effect of aging conditions to the structure of MP formulations containing glyceryl dibehenate (GB) or stearyl alcohol (SA) as matrix formers, and poloxamer 407 alongside the API. SA or GB is used to provide an inert matrix to suspend the API during the melt-spray process. The release of API from the MP occurs via porous diffusion according to the solubility of the drug. 13-15 For the porous diffusion, it is important that the API and poloxamer have low solubility in the SA/GB. Poloxamer 407 is commonly used in pharmaceuticals as a soluble, pore-forming agent that enhances the network of pores and promotes drug dissolution and release, which is especially useful when the solubility or concentration of the API is too low to form a network of pores.<sup>5</sup> The modulation of the concentration of poloxamer 407 allows for modification of the release rate of the API. 16 In the presence of poloxamer 407, the temperature of the formulation during storage has been shown to affect the API release rate, 16 as it is the case also for the level of humidity and any introduction of water during storage. 14,16 For the MPs studied in this work, it was observed that the initial release rate of MPs significantly decreased after aging for 7 months at the conditions of 40°C and 0 % or 75 % relative humidity (RH) (Fig. S1a) with respect to non-aged samples. In contrast no changes in the release rate were observed when MPs were aged for 7 months at lower temperatures of 30°C and 0 % RH or 75 % RH (Fig. S1b), or when at 40°C and 53 % RH (Fig. S1a). In order to gain a better understanding of the changes occurring in the MPs during aging that could explain this behaviour, advanced structural and chemical analysis was performed as described in this work. The formulations studied in this work were manufactured and then aged for 7-8 months at 30-40°C and at 3 different levels of humidity.

Accelerated aging studies generally consist of thermogravimetric analysis (TGA) to determine the thermal stability and differential scanning calorimetry (DSC) for thermal analysis. 16–18 Typical analytical tools employed are Fourier transform infrared (FTIR) spectroscopy and x-ray diffraction (XRD) to measure the chemical properties, scanning electron microscopy (SEM) to measure the size and surface morphology, and high performance liquid chromatography (HPLC) to measure drug content. 6,17,19-21 However, these methods tend to provide information on the materials average bulk properties, while imaging modalities have been shown to be useful to gain structural and chemical insights into the MP systems, Jiang et al.<sup>22</sup> and Qi et al.<sup>23</sup> employed SEM to measure the size and shape of individual MPs and Cape et al.<sup>14</sup> and De Coninck et al.<sup>16</sup> demonstrated the use of SEM to assess the structural properties of MPs. Qi et al made use of confocal laser scanning microscopy (CLSM) to identify chemical entities in the formulation and image their distribution over time.<sup>23</sup> However, this technique required a fluorescent dye for labelling the API, which in itself may affect the behaviour of the API and therefore its final local concentration. Furthermore, the unknown labelling efficiency translates in some level of uncertainty on the distribution of the API. This was to some extent overcome by Bertoni et al, who used Raman spectroscopy mapping to provide information on the lipophilic and hydrophilic phases in a MP.<sup>24</sup> However, this method suffers from long acquisition times and careful consideration is needed to balance a shorter chemical mapping time against a higher lateral resolution of the image.

In this work, we have complemented some of these imaging techniques, namely SEM and Raman spectroscopy, with the state-of-the-

art methods of environmental SEM (ESEM) and stimulated Raman scattering (SRS) microscopy. ESEM provided information on the physical changes as typically measured with SEM, with the additional ability to monitor materials in-situ under specific environmental conditions such as elevated humidity, allowing for physical transformations which occur over long periods of time under ambient conditions to be observed rapidly on the timescale of the experimental measurement.<sup>25</sup> Confocal Raman spectroscopy mapping provided complementary chemical imaging of the surface and cross sections of MPs and was used to identify excipients and the API. Despite the detailed information, confocal Raman mapping suffers from long acquisition times. For this reason, conventional spontaneous Raman spectroscopy was coupled with SRS microscopy, which allowed for rapid chemical imaging of a single Raman wavenumber at a time. SRS microscopy allows for the visualisation of each component with a specific vibrational band in the Raman spectra, which is selected in advance, based on spontaneous Raman spectroscopy measurements of the samples. SRS images can be rapidly acquired at a high spatial resolution, therefore detailed information can be extracted on the size and shape of the API particles, and the distribution of the API and excipients throughout pharmaceutical formulations.<sup>26–28</sup> Owing to its rapid image acquisition speed, SRS was also used to image multiple MPs to study sample variability across a large MP population.

#### **Materials and Methods**

Materials

Glyceryl dibehenate (Compritol ATP 888) was used as purchased from Gattefosse, stearyl alcohol (Kolliwax®) and poloxamer 407 (Kolliphor® 407) were obtained from BASF Corporation and were used as purchased. The API has a melting point of 227.0°C, low solubility, high permeability, is highly crystalline and is non hygroscopic. Full details of the API are not disclosed for proprietary reasons.

#### Multiparticulate Formulations Preparation

A molten mixture was formed of the API, with GB or SA, and poloxamer 407 according to Table 1. It should be noted that samples C and D in Table 1 consist of different batches of nominally identical formulations. The molten mixture was then fed into the centre of a custom-made spinning disk atomizer that consisted of a bowl-shaped stainless-steel disk that was 10.2 cm in diameter. The temperature of the spinning disk atomizer was maintained between 80°C and 95°C by the heat emitted from the molten stream. The rotations of the spinning disk were controlled by a motor mounted below the disk, allowing for speeds of up to 10,000 rpm. Finally, the MSC microspheres were formed when the droplets that were spun off the atomizer congealed in ambient air. Microspheres were collected in an inflated bag.

#### Aging Conditions

The aging conditions are presented in Table 1. For each condition, a representative sample of 60 mg of the MP formulations was placed into glass vials inside an environmental chamber. After aging, vials were removed from each storage condition, and measurements or evaluations were performed. Samples were tested for dissolution (Fig. S1) and characterisation as described in the sections below. The aged samples were left to equilibrate at ambient conditions for up to 24 hours for the dissolution tests and were stored at ambient conditions for up to 2 months for the Raman spectroscopy, SEM and SRS microscopy studies. During storage, no changes were observed in the high resolution imaging by SEM.

**Table 1**Sample names, their composition as a weight percentage, and aging conditions in terms of duration, temperature and relative humidity.

	Formulation						
Sample Name	%GB	%SA	%Poloxamer 407	%API	Duration of aging (months)	Temperature (°C)	Relative humidity (%)
A	40	0	20	40	n/a	n/a	n/a
В	45	0	15	40	n/a	n/a	n/a
B_0RH	45	0	15	40	7	40	0
B_53RH	45	0	15	40	7	40	53
B_75RH	45	0	15	40	7	40	75
B_75RH_30C	45	0	15	40	8	30	75
C	0	45	15	40	n/a	n/a	n/a
D	0	45	15	40	n/a	n/a	n/a
D_0RH	0	45	15	40	7	40	0
D_53RH	0	45	15	40	7	40	53
D_75RH	0	45	15	40	7	40	75

#### Scanning Electron Microscopy (SEM)

Surface morphologies as well as the internal structure of the MP were studied using Zeiss (Germany) scanning electron microscopes (SEMs). For simple imaging of the particles, secondary electron images were acquired in both Supra 40 and Auriga 60 Field Emission SEMs, which were used at 1 kV and with a small aperture giving <20 pA beam current to prevent charging. The samples were prepared by sprinkling them onto a self-adhesive carbon tape. The imaging under controlled environmental conditions was performed in an EVO 50EP SEM instrument, which is a standard tungsten filament SEM in extended pressure mode, with a 500  $\mu$ m final aperture enabling chamber pressures of 2000 Pa and using water vapour to control the humidity surrounding the sample. The sample stage was Peltier cooled and samples were prepared by sprinkling onto copper stubs using conducting carbon cement to embed the particles and ensure good thermal contact. The samples were cooled to 5°C with a water vapour pressure of 1000 Pa to give near 100 % RH. Imaging was performed at 20 kV with a 1 nA beam current and a solid-state backscattered electron detector.

#### Raman Spectroscopy

Confocal Raman spectroscopy measurements were carried out using an inVia Qontor spectrometer (Renishaw plc, UK) with a 50×, 0.5 NA objective lens (Leica Microsystems Ltd, Germany). Raman spectra of the excipients and API were acquired with a 532 nm laser and a power at the sample of 2.5 mW. Raman spectra of the ESEM sample were acquired with a 830 nm laser, a power at the sample of 13 mW to 43 mW, and a line profile spot size of  $\sim\!2~\mu{\rm m}$  in X-axis and 7  $\mu{\rm m}$  in Y-axis. Each spectrum was acquired with 2 accumulations of 30 s. The excipients and API were measured inside glass vials and the laser was focussed >100  $\mu{\rm m}$  into the sample, to allow for contributions from different regions. Three spectra were acquired per sample at different locations and subsequently averaged for each sample.

Transmission Raman spectroscopy measurements were acquired with a 830 nm laser and a 50×, 0.5 NA objective lens (Leica Microsystems Ltd, Germany), a power at the sample of 92 mW, and a spot size of >100  $\mu$ m. Three spectra were acquired per sample at different locations with two acquisitions of 60 s per spectrum and subsequently averaged for each sample. Samples were measured inside glass vials.

Surface maps were acquired with a 532 nm laser and a  $100\times$ , 0.9 NA objective lens (Leica Microsystems Ltd, Germany), a power at the sample of 2.2 mW, and a spot size of  $\sim$ 1  $\mu$ m. The samples were sprinkled onto a self-adhesive carbon tape. Cross section maps were acquired with a 532 nm laser and a 50 $\times$ , 0.5 NA objective lens, a power at the sample of 2.5 mW, and a spot size of  $\sim$ 1.5  $\mu$ m. The samples were sprinkled onto a silicon wafer using conducting carbon

cement to embed the particles, then cut with a scalpel blade. The 'LiveTrack' feature of WiRE software (Renishaw plc, UK) maintained the focus for the surface maps (Fig. S2) throughout the measurement to correct for differences in the Z-axis position of the surface due to the curvature or roughness of the MP and allowed for a clear image. Maps were all acquired with a 1  $\mu$ m pixel spacing, with 1 acquisition of 3 s per spectra at each pixel.

Analysis was carried out in WiRE version 5.4 and the spectra were baseline corrected with an intelligent polynomial of order 9 to 11. Any cosmic rays were removed with a 'Width of Features' algorithm (single spectra) or a 'Nearest Neighbour' algorithm (maps). For analysis of the maps, direct classical least squares (DCLS) component analysis was used to fit each ingredient to the spectra. Confocal Raman spectra and spectra from surface maps were calibrated to the 520.5 cm<sup>-1</sup> peak from a silicon sample. The transmission Raman spectra were calibrated to a confocal Raman spectrum of sample B acquired with the same 830 nm excitation laser wavelength.

## Stimulated Raman Scattering (SRS) Microscopy

SRS microscopy measurements were performed with a Leica SP8 microscope (Leica Microsystems Ltd, Germany). A PicoEmerald-S laser system (APE, Berlin) was used to output two pulsed 2 ps laser beams; a 1031 nm Stokes beam spatially and temporally overlapped with a tuneable pump beam. The Stokes beam was modulated at 20 MHz and stimulated Raman loss signals were detected in transmission using a silicon-based detector and lock-in amplifier (UHFLI, Instruments, Switzerland). A water immersion 25× magnification objective lens (0.95 NA, Leica Microsystems Ltd, Germany) and a long working distance air condenser lens (0.55 NA, Leica) were used due to the sample thickness. A laser power of  $\sim$ 14 mW for the pump beam and  $\sim$ 39 mW for the Stokes beam at the sample was used. Image acquisition was performed using Leica LAS-X version 3.5.5.19976, which was also used for image analysis in combination with ImageJ (Fiji). The field of view was 465  $\mu$ m, therefore for larger areas tile scans were performed where an array of multiple images was collected and combined using the 'mosaic merge' function within Leica LAS-X. The images acquired at each position for each ingredient were overlayed in ImageJ 29. For MP counting, a threshold and gaussian blur were applied on the tile scans for each ingredient and the maxima were found in ImageJ, using the 'Find Maxima' function.

Confocal Raman spectra guided the selection of the wavelengths for SRS microscopy measurements. A Raman shift of 1401 cm<sup>-1</sup> was chosen to identify the API, and 1303 cm<sup>-1</sup> for the identification of the GB, while 1279 cm<sup>-1</sup> was chosen to check the off-resonance signal to confirm the signals vanished when tuned away from a peak and could therefore be confirmed to be Raman scattering rather than

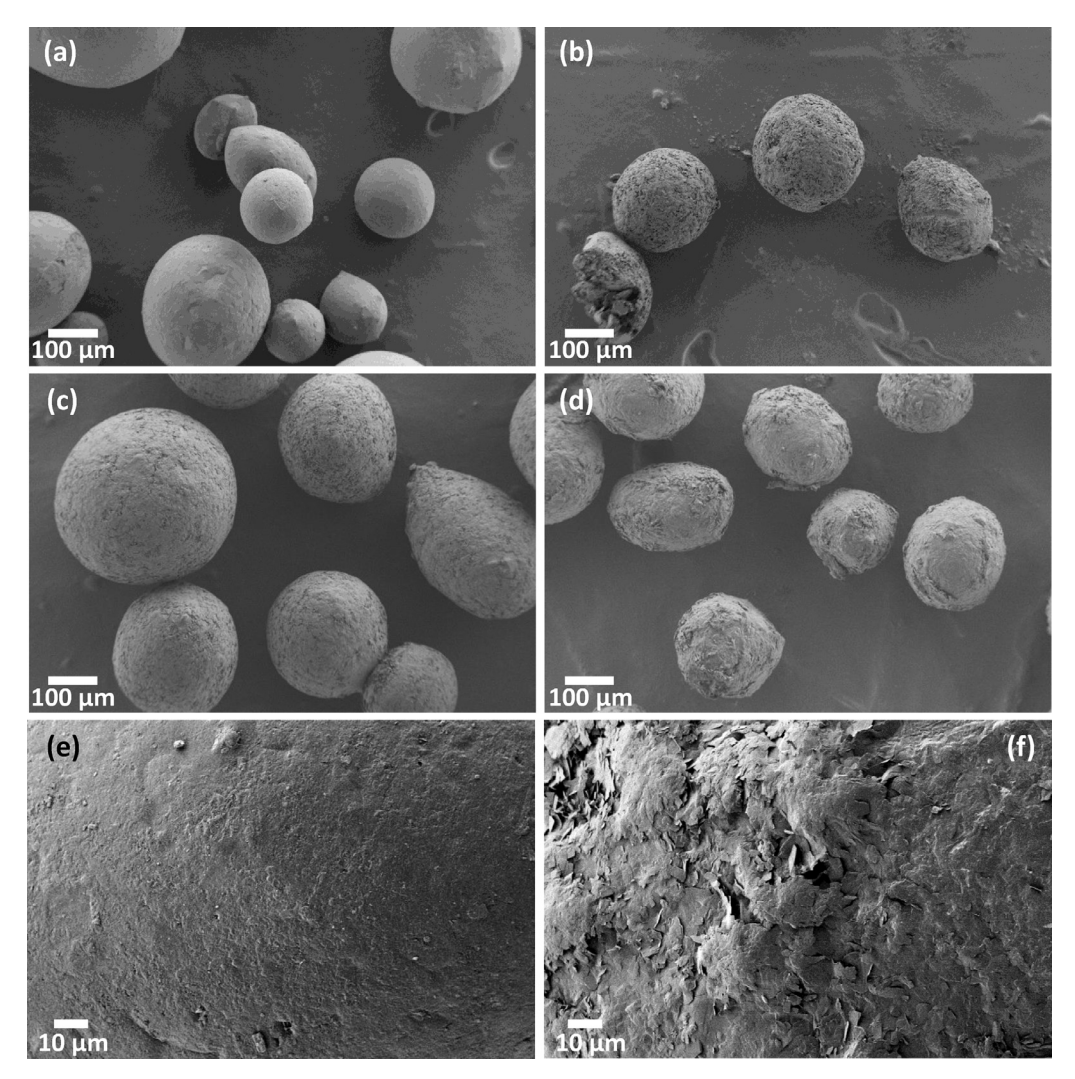


**Figure 1.** Representative SEM images of batch B with (a) no aging, and after aging for 7 months at 40°C with a relative humidity (RH) of (b) 0 %, (c) 53 % and (d) 75 %. Higher magnification SEM images of batch B after aging at 75 % RH for (e) 8 months at 30°C and (f) 7 months at 40°C. Additional images comparing changes in RH can be found in the supplementary information (Fig. S6).

spurious signals <sup>30</sup>. An off-resonance image was acquired as a control measurement (Fig. S3b and d, Fig. S4b and Fig. S5b), at a wavelength not attributed to any ingredient, and has been subtracted from the on-resonance images in Fig. 6 and Fig. 7 in order to remove minor spurious signals.

#### Results

#### Morphology of the MPs

Characterisation of structural features of the MP was carried out to map and understand possible changes in the surface morphology and topology of the MPs as a result of the aging process. Fig. 1 shows SEM images of MP formulation B samples which were aged under different conditions. The size of the non-aged MPs ranged between  $\sim 100~\mu m$  and  $\sim 400~\mu m$  (Fig. 1a) and their shape was typically close-to-spherical with a smooth surface. Some particles deviated significantly from a spherical geometry, exhibiting a drop-shape appearance. After aging at 40°C for 7 months, the MP size appeared similar to the non-aged particles, however there were clear changes in the surface morphology. The samples aged at 0 % RH and 53 % RH exhibited surface features suggesting the presence of pores at the surface (Fig. 1b and 1c). Upon aging at 75 % RH, fewer "pores" were visible on

the MP surface, however the surface appeared rougher (Fig. 1d) and very different to the smooth structure seen in the non-aged sample (Fig. 1a). Upon aging at lower temperatures of 30°C, the MP surface changes were less apparent (Fig. 1e), compared to the samples aged at 40°C (Fig. 1f) at the same humidity of 75 % RH. This is consistent with the dissolution profiles (Fig. S1) where there was a significant decrease in initial release rate for the sample aged at 40°C at 75 % RH, but not the sample aged at 30°C at 75 % RH.

## Raman Spectroscopy Measurements

Raman spectra of each excipient and API are shown in Fig. 2a and were used to identify the chemical compounds associated with the peaks observed within the Raman spectra of the formulations. The Raman spectra of GB and poloxamer 407 were consistent with the literature. <sup>17,31</sup> For each compound, the spectra exhibited one or more unique peaks that could be used for chemical identification, namely an intense peak at 1401 cm<sup>-1</sup> for the API, an intense peak at 1296 cm<sup>-1</sup> for the GB and SA, and a peak at 843 cm<sup>-1</sup> for the poloxamer 407. Though, the lower relative concentration of poloxamer 407 and lower intensity of the unique peak meant that, in practice, no specific peak could be used to create a map of its distribution, and therefore DCLS analysis was used to calculate the contribution of each

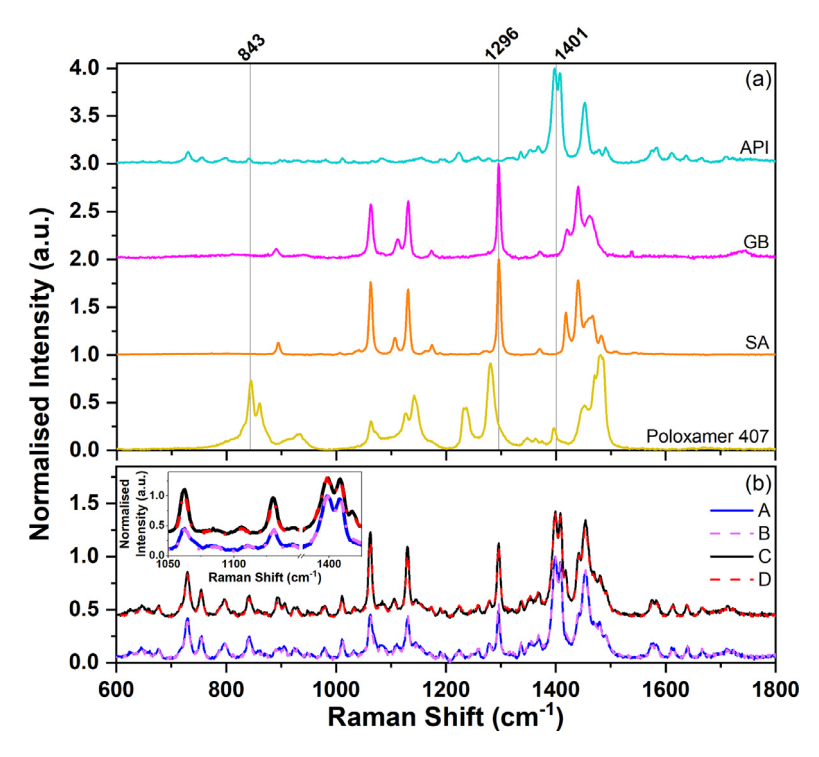


Figure 2. (a) Confocal Raman spectra of API (cyan), GB (magenta), SA (orange) and poloxamer 407 (yellow), acquired with a laser wavelength of 532 nm. The vertical lines show the peaks initially selected for chemical identification. (b) Transmission Raman spectra of samples A (blue), B (purple), C (black) and D (red), where A and B contain GB, and C and D contain SA. An inset is shown to aid the visualisation of differences between samples. Each spectra is an average of 3 measurements per sample, aquired over 2 accumulations of 30 s, with transmission Raman spectra acquired at a laser wavelength of 830 nm. All spectra were normalised to the maximum intensity. All samples were non-aged.

ingredient to the overall spectrum. This enabled the calculation of the relative concentration of poloxamer 407 across the image to produce the relative chemical map.

Fig. 2b shows the spectra of samples A, B, C and D, as measured by transmission Raman spectroscopy. In this method, the beam is expanded and analyses much larger sample volumes, enabling the measurement of Raman signal to be representative of the bulk chemistry of the materials.<sup>32</sup> This allows for a rapid and straightforward evaluation of the overall composition of the sample, for comparison with other batches, which is particularly useful to avoid sub sampling when samples contain multiple components with microscale variations in concentration. Formulations A and B resulted in similar spectra, with similar relative intensities of the GB and API. This appears to suggest that the 5 % difference in the mass of poloxamer 407 between samples A and B is below the sensitivity of the method and cannot be detected by transmission Raman spectroscopy. As expected, samples C and D had similar Raman spectra because of their nominally identical composition (Table 1).

The formulations with GB (A and B) both have a similar peak intensity ratio at  $1062~\rm cm^{-1}$  compared to  $1130~\rm cm^{-1}$ , attributed to trans chain C-C stretching out-of-phase and in-phase vibrations, respectively. The formulations containing SA (C and D) have a higher peak intensity at  $1062~\rm cm^{-1}$  than at  $1130~\rm cm^{-1}$ , which is different to the samples containing GB, due to the slight differences in molecular structure. The ratio of the SA and GB peaks ( $1062~\rm cm^{-1}$ ,  $1130~\rm cm^{-1}$  and  $1296~\rm cm^{-1}$ , where the latter is the in-plane CH<sub>2</sub> twist<sup>33,34</sup>) to the API is higher in the samples containing SA despite having a similar concentration to the GB, which is unsurprising as these are different excipients with differences in molecular structure and overall proportion of carbon chains.

Fig. 3a shows the confocal Raman mapping of the cross section of a representative single MP from batch A (no aging). Each image pixel contains information on the full Raman spectrum associated with the material at that location. These spectra were analysed to identify the

material's chemical composition, whose information is rendered in the image by associating specific colours with the different chemistries. The API (cyan) appears to be distributed in particles throughout the MP. GB (magenta) can be seen to surround the API and be present throughout the MP. The poloxamer 407 was present in small quantities in different regions of the cross section. The different ingredients can be associated with structural features observed in the related optical image (Fig. 3b). The ability to associate structural features to specific chemistries significantly enriches the information delivered by the imaging methods, enabling interpretation of morphological features in relation to their chemistry.

For batch B, we performed an extended complementary analysis of the chemical and morphological features of the surface of the MPs before and after aging, by comparing confocal Raman mapping with SEM imaging, as shown in Fig. 3c to 3h. For the non-aged sample, the Raman spectroscopy map (Fig. 3c) identified GB as the main component. This formed the smooth surface imaged by SEM (Fig. 3d), along-side areas attributed to poloxamer 407. The Raman spectroscopy maps also suggested the geometrical features occasionally apparent in the SEM images corresponded to the API particles.

As observed previously, Fig. 3e and 3f show that upon aging at 0 % RH, the MP surface lost the smooth appearance which was observed in the non-aged sample, to exhibit a flaky structure attributed to the GB, similar to one of the typical forms (unctuous flakes) of GB.<sup>35</sup> No presence of poloxamer 407 was observed after sample aging, but the API was still present as particles in different regions across the surface.

Upon aging at 75 % RH, the GB appeared as rough features at the surface, as shown by Fig. 3g and h. The presence of poloxamer 407 was observed in a very low concentration. However, the API still appeared as particles and was present in different regions across the surface.

The average spectra of the surface maps in regions with low API local concentration (i.e. DCLS component of <0.03), showed some changes after aging. The non-aged sample exhibited a shoulder peak

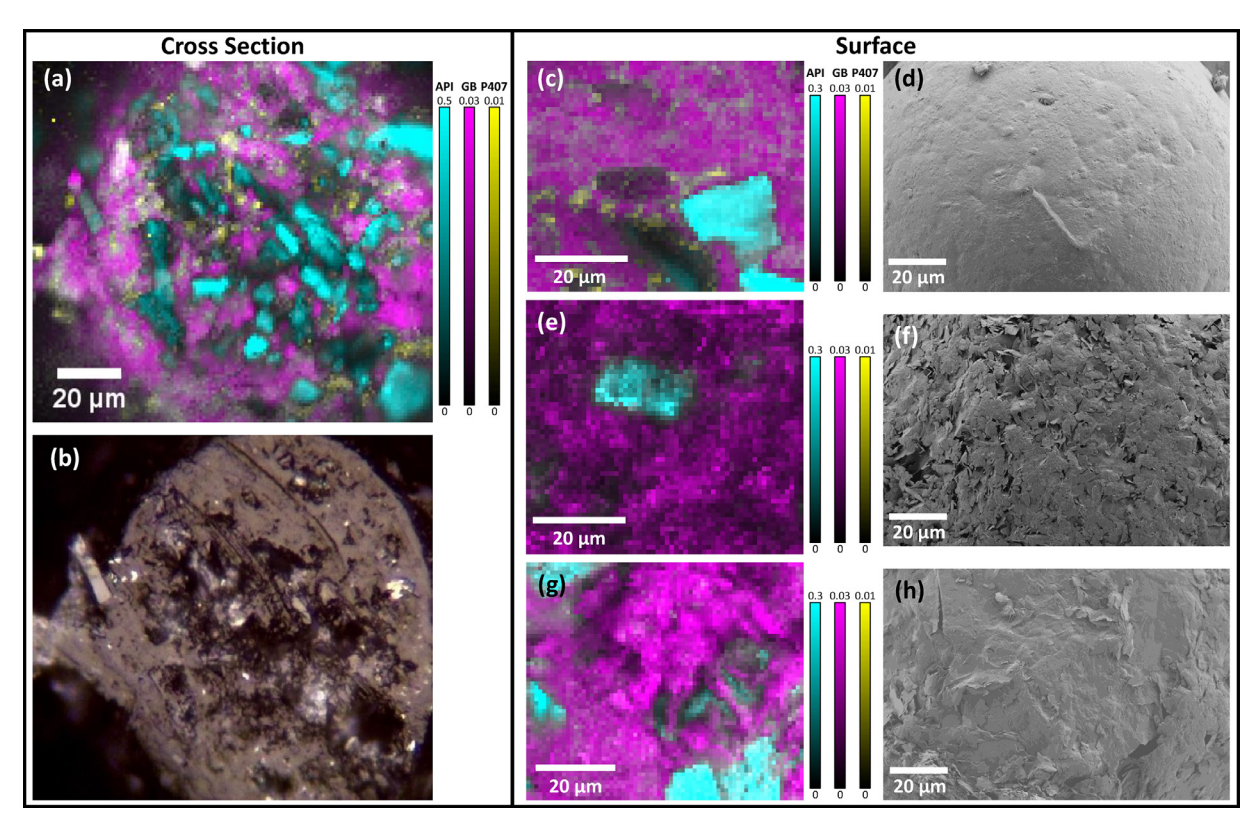


**Figure 3.** (a) Raman spectroscopy map and (b) optical image of the cross section of a MP from batch A (no aging) after cutting in half with a scalpel. Raman spectroscopy maps and SEM images of the surface of a MP from batch B with (c, d) no aging, and after aging for 7 months at 40°C with a relative humidity (RH) of (e, f) 0 %, and (g, h) 75 %, respectively. The API is in cyan, the GB is in magenta, and the poloxamer 407 is in yellow.

around 1280 cm<sup>-1</sup> consistent with the presence of poloxamer 407, whereas the aged samples did not exhibit this peak (Fig. S7a) suggesting a reduced local concentration or absence of poloxamer 407. This appears consistent with the changes observed in the intensity ratio of the peaks at 1062 cm<sup>-1</sup> and 1130 cm<sup>-1</sup> in the aged and nonaged samples, as Fig. 2a shows that both the GB and poloxamer 407 are expected to contribute to the intensity of the peak at 1130 cm<sup>-1</sup>. However, it can not be excluded that the differences observed in the peak intensity ratio are due to different relative concentrations of glyceride forms (mono, di and triglycerides), or to the degradation of these forms.<sup>36</sup> It is known, in fact, that when poloxamer 407 is present in concentrations >10 %, it may have an effect on the miscibility of a small fraction of GB, and is preferentially miscible with monoglycerides,<sup>36</sup> therefore the loss of poloxamer 407 could explain changes to the relative concentration of each GB form. More significantly, the aged samples exhibited an additional peak at 1730 cm<sup>-1</sup> (Fig. S7a), which is consistent with carbonyl-containing oxidation products that may have been generated during the aging process.<sup>36,37</sup> The peak at 1730 cm<sup>-1</sup> did not occur at every position, even within a single sample (Fig. S7b).

In the formulation of sample D, poloxamer 407 (yellow in Fig. 4) and SA (magenta) were observed at the surface of the MP. The latter, which substitutes GB in the formulation, similarly appeared to surround the API (Fig. 4a, 4b and 4g). Raman spectroscopy maps of the cross sections of batch C and batch D before any aging appear very similar, which is as expected due to the identical nominal composition of the two batches. After aging at 0 % RH, the surface of sample D significantly changed (Fig. S8 and Fig. S9) with smooth flake-like features covering the MP. Corresponding Raman spectroscopy maps and SEM images from the same region allow for the identification of SA as the excipients causing these flakes. Fig. 4(i), in fact, suggests the API are still geometrically shaped, whereas the SA formed additional

features on the surface. After aging at the higher relative humidity of 75 %, poloxamer 407 appeared to enrich the surface of the MP (Fig. 4f and 4k). Cross sectional images of sample D were particularly useful when investigating the location of different excipients. While Fig. 4k shows a low concentration of SA at the surface, Fig. 4f suggests SA is still present inside the MP. On the contrary, Fig. 4d shows that in samples aged at 0 % RH there is a low concentration of poloxamer 407 throughout the whole MP as well as at the surface.

## Environmental SEM (ESEM) Analysis

To gain further insights into the chemical and structural changes induced on the formulations by aging, non-aged MPs from batch B were monitored with SEM in an environmental chamber, under conditions designed to simulate an accelerated aging process. The typical outcome of these measurements is shown in Fig. 5. Fig. 5a shows a MP before any accelerated aging, at a water vapour pressure of 100 Pa (12 % RH). The water vapour pressure was subsequently increased over a duration of 39 minutes to reach a value of 1000 Pa (100 % RH). This timepoint was labelled as "0 minutes", after which the MP was carefully monitored. Between 0 (Fig. 5b) and 17 (Fig. 5f) minutes, the MP gradually increased in size, with a 9 % increase in the radius; for clarity, in each subfigure of Fig. 5 the projected circumference of the MP at Fig. 5a before aging is marked by a red line, while the current one is marked by a blue line. After 5 minutes at 1000 Pa (Fig. 5c), we observed a droplet that had formed on the surface on the MP and after 32 minutes (Fig. 5g) a smooth material or solution covering the surrounding region. From this timepoint onwards, the water vapour pressure was decreased and at 40 minutes (Fig. 5h) reached a pressure of 100 Pa (12 % RH). At 40 minutes the MP appeared to have contracted slightly towards the original size, while the surrounding material observed at 32 minutes was still present.

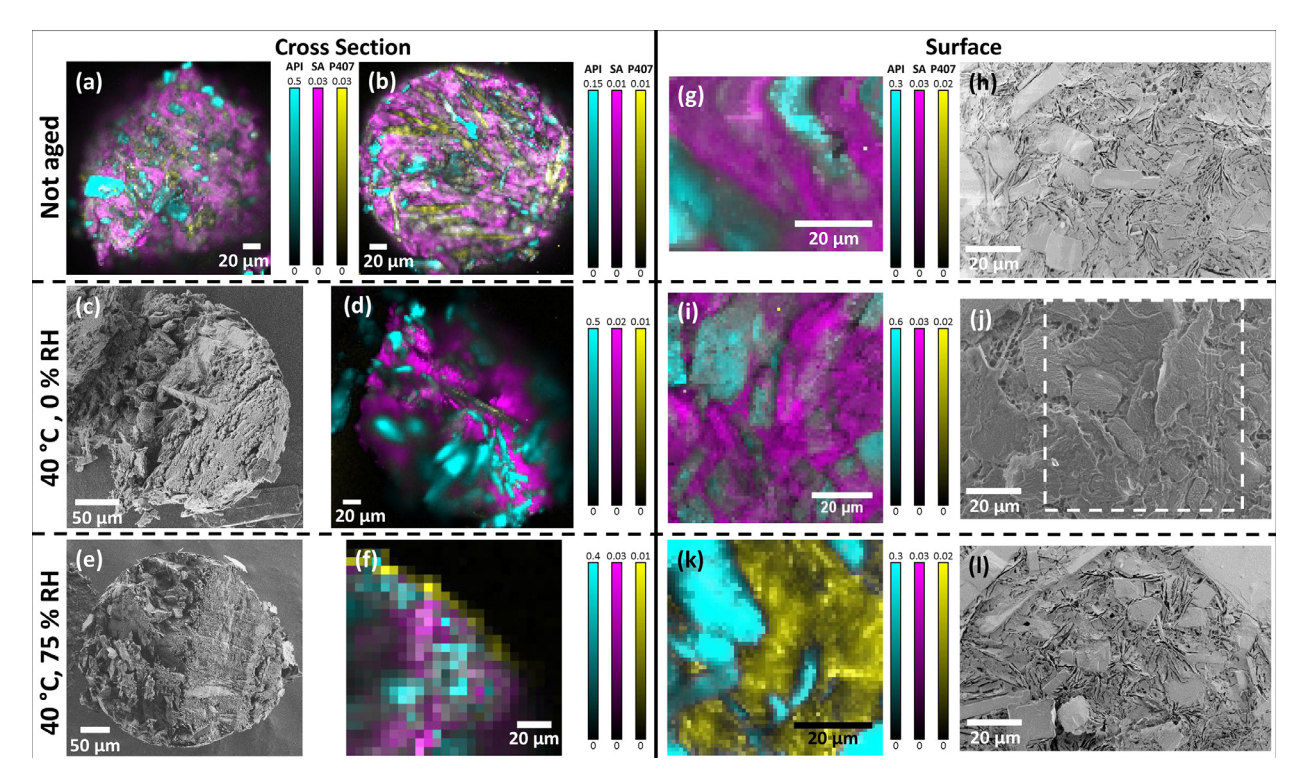


**Figure 4.** Raman spectroscopy maps (a, b, d, f) and SEM images (c, e) of the cross section of a MP after cutting in half with a scalpel. Images were acquired from (a) batch C (no aging), (b) batch D (no aging), and batch D after aging for 7 months at 40°C with a relative humidity (RH) of (c, d) 0 %, and (e, f) 75 %, respectively. Raman spectroscopy maps (g, i, k) and SEM images (h, j, l) of the surface of a MP from batch D with (g, h) no aging, and after aging for 7 months at 40°C with a RH of (i, j) 0 %, and (k, l) 75 %, respectively. The square in (j) marks the Raman map region in (i). The API is in cyan, the SA is in magenta, and the poloxamer 407 is in yellow.

Raman spectroscopy measurements of the MP in Fig. 5h were used to chemically identify the structural features observed by ESEM and provide insights into the components responsible for the changes. The Raman spectrum measured at position 1 of Fig. 5h is shown in blue in Fig. 5i and appears similar to the transmission Raman spectrum in Fig. 2b, suggesting little change in overall average chemical composition. The Raman spectrum at position 2 was measured at 3 different places on and near the droplet which had formed and dried. The corresponding Raman spectra all exhibited a higher background signal than position 1 (before baseline subtraction) and the ratio of the peaks at  $\sim 1400~\text{cm}^{-1}$  and  $1410~\text{cm}^{-1}$  slightly changed with respect to the spectrum at position 1. This may be due to a chemical change in the API molecule, or an adventitious chemical species deposited during the ESEM analysis. The Raman spectrum of the material surrounding the MP (Fig. 5i, spectrum 3) was predominantly composed of aqueous poloxamer 407.31

## SRS Microscopy Characterisation

The selection of specific Raman shifts in SRS means that MP images can be acquired significantly faster with respect to confocal Raman spectroscopy imaging, where each pixel is associated with a full Raman spectrum. This makes SRS microscopy particularly suited to measure the materials at different depth positions, or over large areas. Images in Fig. 6 are the result of SRS images acquired from the surface of the MP to 53  $\mu$ m inside it along a vertical axis perpendicular to the plane of view, at 1  $\mu$ m increments. Images at further depths were not collected due to insufficient signal to noise caused by signal attenuation from light scattering and absorption by the sample. Fig. 6a shows a maximum projection image of the depth stack and provides a high-resolution representation of the API particles and surrounding GB. It should be noted that poloxamer 407 could not be imaged with SRS because the Raman spectrum did not have a unique

Raman band of high intensity and its relative concentration was low. The image shows that the API is present throughout the MP and the API particles range in size from over 50  $\mu m$  in length, to under 10  $\mu m$ . Both the API and GB were present at the surface of the MP (Fig. 6b) as well as  $\approx$  13  $\mu m$  inside (Fig. 6c). The large number of API particles and surrounding GB can be visualised clearly when separated out into images of the individual components (Fig. 6d and Fig. 6e respectively), and the results are consistent with the confocal Raman spectroscopy maps.

SRS microscopy tile scans consist of a mosaic of several fields of view stitched together, acquired by rastering across the sample. This allows the rapid imaging of many MPs and therefore the study of the distribution of API and GB within them across a large population of MPs. A tile scan at one Z-axis position (Fig. 7) suggested the MPs appear to be mainly spherical, with a few instances of elongated or broken MPs. After applying a threshold and gaussian blur on the separate API and GB tile scan images, the maxima can be identified in ImageI to give the number of MPs (Fig. S10) and calculate the percentage containing API. In the GB component of Fig. 7 225 MPs were identified as containing GB, and in the API component of Fig. 7 225 MPs were identified as containing API. These figures exclude broken MPs and are corrected for parts of elongated MPs that were erroneously counted as individual particles. The 225 MPs that were identified contained both API and GB, suggesting API is present in 100 % of the MPs.

## Discussion

The MP formulations were characterised using advanced microscopy methods for the analysis of their behaviour upon aging. It was demonstrated that control over environmental conditions for SEM and chemical mapping with live tracking of the focus for Raman spectroscopy provided deeper insights into the chemical structure of the

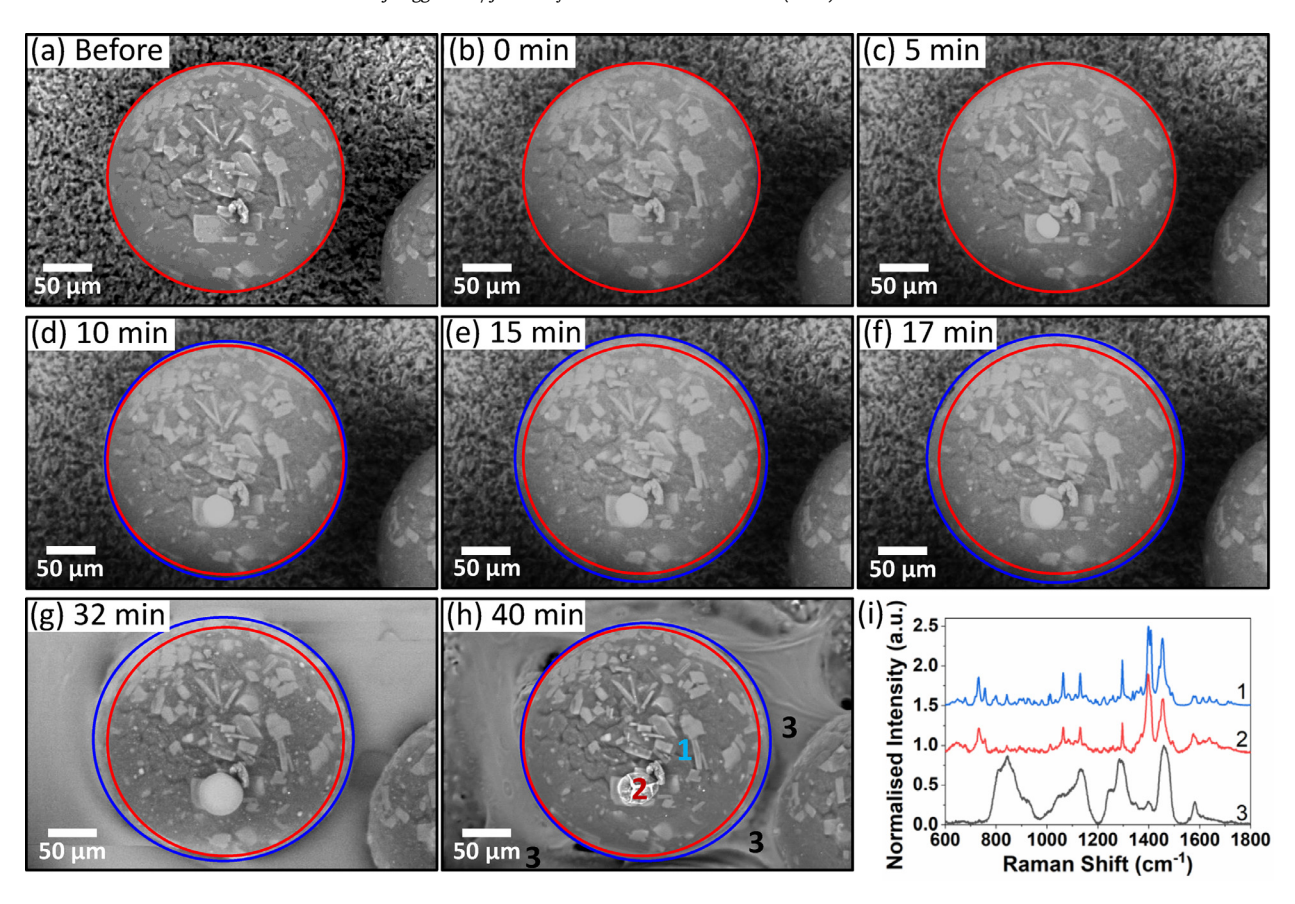


Figure 5. Environmental scanning electron microscopy (ESEM) of batch B without previous aging. The water vapour pressure was increased to 1000 Pa over 39 minutes between (a) 'before' and (b) '0 min'. The water vapour pressure was kept at 1000 Pa bewteen (b) '0 min' and (g) '32 min'. The sample was left to dry between (g) '32 min' and (h) '40 min'. The sample was mounted on a peltier stage which was kept at  $5^{\circ}$ C throughout the measurments. (i) Raman spectra measured at the positions labelled in (h). Spectra 2 and 3 are each an average of 3 spectra, where the spectra have been taken from the points labelled in (h) and baseline corrected before averaging. The peak at  $\sim$ 1580 cm-1 is most likely from the carbon cement below the sample  $^{38}$ .

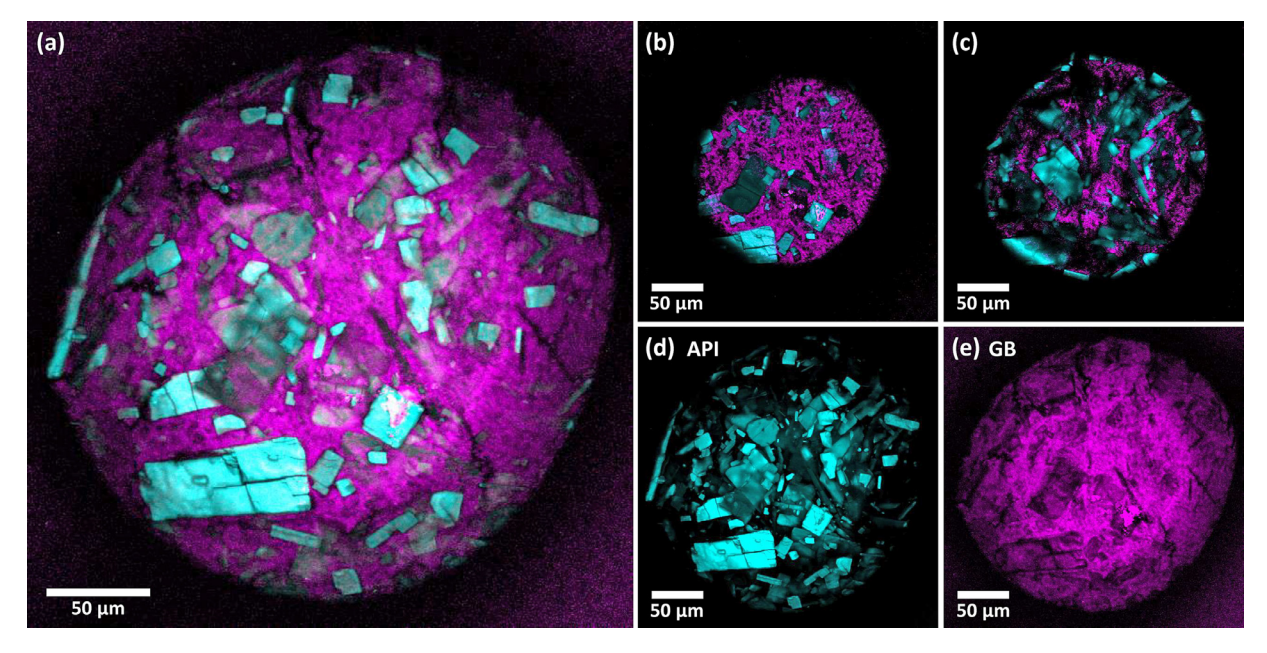


Figure 6. Stimulated Raman scattering (SRS) microscopy (a) maximum projection image of the API and GB. Image of (b) the top  $\approx 1~\mu$ m of the particle and (c) image at a depth of  $\approx 13~\mu$ m into the MP (depth resolution  $\approx 1~\mu$ m). Maximum projection image of (d) the API, and (e) GB. All images are of sample batch B, with the API component (cyan) acquired at 1401 cm<sup>-1</sup> and GB component (magenta) acquired at 1303 cm<sup>-1</sup>.

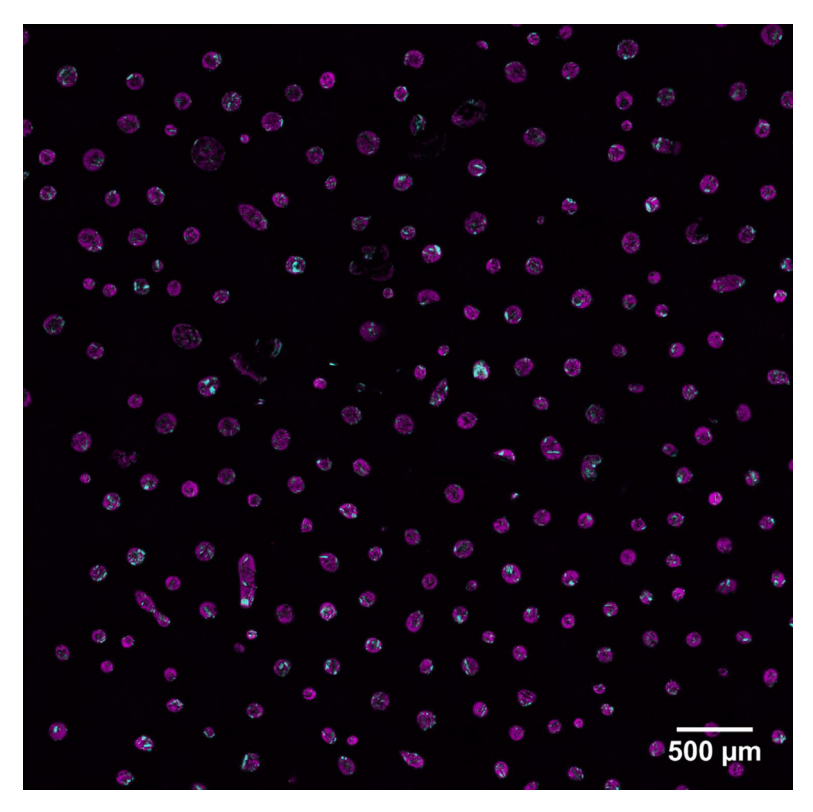


Figure 7. SRS tile scan of MPs from sample batch B, with the API component (cyan) acquired at 1401 cm<sup>-1</sup> and GB component (magenta) acquired at 1303 cm<sup>-1</sup>.

MPs with respect to traditional SEM and Raman spectroscopy methods. These novel capabilities enabled us to study chemical and structural changes of the MPs during aging and across batches of MPs with different formulations. In particular, the ESEM allowed us to study the behaviour of the MPs when exposed to increasing levels of humidity. Combining electron and Raman microscopies enabled the mapping of the distribution of the chemical components across single MPs and the chemical identification of specific morphological features. This was particularly insightful when comparing different MP formulations, i.e. samples B and D, as the presence of SA correlated to a high relative surface concentration of poloxamer 407 at 75 % RH, but the relative surface concentration of poloxamer 407 was very low for the same aging conditions when MPs contained GB. Interestingly, it was also observed that the Raman spectrum and shape of the API particles appeared to be largely unaffected by the aging process. The transmission Raman spectra also allowed the comparison of batch A and B with GB to batch C and D with SA and the technique could be used for relative comparisons of concentrations and batches during manufacturing, for ingredients that are present in concentrations above the limit of detection of the method.

Raman spectroscopy maps such as Fig. 3a are very useful for determining the distribution of the different chemical components in the samples and correlating with morphological features. The large Raman shift range and high spectral resolution  $(3-4~{\rm cm}^{-1})$  of the confocal Raman spectroscopy maps are particularly useful if the Raman spectra of the individual excipients and API do not have unique Raman bands, as the identification of these chemical components would be challenging from a single Raman shift or with the poorer spectral resolution of SRS ( $\sim 10~{\rm cm}^{-1}$ ). In this work, the poloxamer 407 did not have a unique Raman band of high intensity and was present in low concentrations compared to the other components, therefore the confocal Raman maps were useful to show this component. However, Raman spectroscopy maps can take hours or even days to acquire, depending on the total sample area and the lateral

resolution of the image. SRS microscopy is a complementary Raman technique which allows for faster measurements at specified Raman shifts, with improved axial resolution ( $\sim\!1~\mu\mathrm{m}$ ) compared to confocal Raman ( $\geq\!5~\mu\mathrm{m}$ ). This technique enabled more rapid chemical mapping at high spatial resolution of both the surface and the inner volume of the MPs with minimal sample preparation. The rapidity of the method also meant we could image large areas (tile scans) of the sample for measuring the overall population of MPs, which can be used to help quantify the number of MPs containing API. In this work, the SRS tile scans confirmed the presence of API in 100 % of the MPs imaged from sample batch B. The SRS tile scan in this work was measured at one Z-axis position, therefore it is more suitable for comparing variability rather than quantifying the size of the MPs.

As far as the formulation containing GB is concerned, the SEM images performed before and after aging under different conditions suggested that the changes observed in the MPs depend upon the level of relative humidity present during storage. Both of the aged samples exhibited changes in the Raman spectra at locations with high GB concentration, which appears to suggest a possible degradation of the GB. An investigation into the surface morphology of the aged MPs showed the MPs remaining a similar size to the non-aged sample, but pores forming at 0 % RH, which suggests that part of the MP was lost while the macroscopic structure remained unchanged. This is consistent with the loss of poloxamer 407 observed in the Raman spectroscopy map at the surface of the MP stored at 0 % RH, which may have contributed towards the formation of these pores. In contrast, upon aging at 75 % RH the MPs also remained a similar size to the non-aged sample, but the GB on the surface appeared very rough and a smaller number of surface pores were observed.

The ESEM method enabled us to directly observe the effect of changes in relative humidity on the structure of the MPs. The controlled introduction of water vapour while maintaining a constant temperature was coupled with the simultaneous imaging. The main structure of the MPs was observed to expand with the increase in

humidity and contract upon drying. During this process, we observed the accumulation of aqueous poloxamer 407, as confirmed by Raman spectroscopy, around the MPs. The migration of poloxamer 407 had also been observed in the Raman maps of the samples aged for 7 months. This appears to suggest that poloxamer 407 may leak out of the MP, while the Raman maps also suggested GB may change to a different form. Poloxamer 407 promotes drug dissolution and release, therefore the loss of poloxamer could be the cause of the change of the release rate that was observed upon aging (Fig. S1). It can not be excluded, however, that the difference in the release rate is also due to changes in the GB polymorphic forms.<sup>36</sup>

The formulation containing SA highlighted the importance of utilising cross-sectional mapping of MPs alongside surface mapping. While the sample aged at 0 % RH showed a loss of poloxamer 407 similar to the GB formulation, the sample aged at 75 % RH exhibited a high relative surface concentration of poloxamer 407, different to the GB formulation. The Raman spectroscopy map of the cross section at 75 % RH confirmed the presence of SA in the core of the MP, despite the very low SA concentration at the surface. These results allowed us to identify the migration of different excipients within the MP.

The methods investigated in this work complement routine tests performed on these types of MPs. When used in conjunction with release test profiles, these methods can help identify the optimal formulation and optimise the production and storage methods for prolonging the lifetime of MPs.

#### **Conclusions**

MP formulations containing GB, SA and poloxamer 407 were characterised to study the changes to structure morphology and distribution of the formulation ingredients due to the exposure to different environmental conditions over 7 months. The insights discovered with advanced Raman spectroscopy-based methods and ESEM inform the formulation and manufacturing of the MPs and support further development. We have shown the utility of these methods to study pharmaceutical formulation aging under a range of storage conditions and help to form a basis of understanding on the aging process.

In this instance, we have confirmed the presence of API in all the MPs that were measured, identified as different sized particles. The topography of GB and concentration of poloxamer 407 at the surface of the MP was found to change in MPs whose release rate decreases significantly after aging for 7-8 months at 40°C and 0 % RH or 75 % RH. The results suggest that the loss or reduction in poloxamer 407, possibly due to solid form transformations of GB where the poloxamer 407 is miscible, may be one of the causes of the decrease in release rate, which is consistent with the knowledge that poloxamer 407 is used to promote drug dissolution and release rate. We have discussed that the change in release rate could also be due to the potential GB polymorphic form transformations ocurring during aging. In the case of the formulations containing SA, after aging at 40° C for 7 months, the humidity conditions also appeared to affect the behavior of poloxamer 407, with a significant difference in its surface concentration observed at 75 % RH compared to 0 % RH.

Future work could see these methods used in a larger range of pharmacuetical products and compared directly with the bulk properties measured with techniques such as TGA and HPLC.

#### **Declaration of competing interest**

The authors declare that they have no known competing financial interests or personal relationships that could have appeared to influence the work reported in this paper.

#### **CRediT authorship contribution statement**

Elizabeth J. Legge: Formal analysis, Methodology, Writing – original draft. Mark Stewart: Formal analysis. Lourdes P. Contreras Chávez: Writing – review & editing, Investigation, Methodology. Hannah Zhang: Formal analysis. Dimitrios Tsikritsis: Writing – review & editing, Formal analysis. Natalie A. Belsey: Supervision, Writing – review & editing, Mark McAllister: Supervision, Methodology. John Richard Murphy: Supervision, Methodology. Ken Mingard: Supervision, Writing – review & editing, Formal analysis. Caterina Minelli: Conceptualization, Project administration, Supervision, Writing – review & editing, Methodology.

#### Acknowledgements

This work was funded by the UK Department for Science, Innovation and Technology through the National Measurement System Programme.

Support by the Community for Analytical Measurement Science is also gratefully acknowledged for a 2020 CAMS Fellowship Award to Natalie Belsey funded by the Analytical Chemistry Trust Fund.

The authors also thank Dr Vasundhara Tyagi at NPL for discussions related to the manuscript.

#### **Supplementary Materials**

Supplementary material associated with this article can be found in the online version at doi:10.1016/j.xphs.2024.05.004.

#### References

- Sohail Arshad M, Zafar S, Yousef B, et al. A review of emerging technologies enabling improved solid oral dosage form manufacturing and processing. *Adv Drug Deliv Rev.* 2021;178: 113840. https://doi.org/10.1016/j.addr.2021.113840.
- Silva BS, Santangelo M, Colbert M-J, et al. Building process understanding of fluid bed taste mask coating of microspheres. AAPS PharmSciTech. 2019;20(173). https:// link.springer.com/article/10.1208/s12249-019-1384-1#citeas.
- Banerjee S, Joshi U, Singh A, Saharan VA. Lipids for taste masking and taste assessment in pharmaceutical formulations. Chem Phys Lipids. 2021;235(105031). https://www.sciencedirect.com/science/article/abs/pii/S0009308420301626.
- Kushwah V, Lopes DG, Koutsamanis I, et al. Evolution of the microstructure and the drug release upon annealing the drug loaded lipid-surfactant microspheres. Eur J Pharm Sci. 2020;147: 105278. https://doi.org/10.1016/J.EJPS.2020.105278.
- Mehio N, Frericks Schmidt HL, Wood GPF, et al. Binary isobaric phase diagrams of stearyl alcohol-poloxamer 407 formulations in the molten and solid state. *Int J Pharm.* 2022;623: 121908. https://doi.org/10.1016/J.IJPHARM.2022.121908.
- KH Al Zahabi, Ben Tkhayat H, Abu-Basha E, Sallam AS, Younes HM. Formulation of lipid-based tableted spray-congealed microparticles for sustained release of vildagliptin: in vitro and in vivo studies. *Pharmaceutics*. 2021;13(12). https://doi.org/ 10.3390/pharmaceutics13122158.
- Garnero C, Zoppi A, Aloisio C, Longhi MR. Technological delivery systems to improve biopharmaceutical properties. In: Grumezescu AM, ed. Nanoscale Fabrication, Optimization, Scale-Up and Biological Aspects of Pharmaceutical Nanotechnology. William Andrew Publishing; 2018:253–299. https://doi.org/10.1016/B978-0-12-813629-4.00007-3.
- Waterman KC, Adami RC. Accelerated aging: prediction of chemical stability of pharmaceuticals. *Int J Pharm*. 2005;293(1-2):101–125. https://doi.org/10.1016/j. ijpharm.2004.12.013.
- Yawalkar AN, Pawar MA, Vavia PR. Microspheres for targeted drug delivery- a review on recent applications. J Drug Deliv Sci Technol. 2022;75: 103659. https://doi.org/10.1016/j.jddst.2022.103659.
- Bertoni S, Albertini B, Passerini N. Spray congealing: An emerging technology to prepare solid dispersions with enhanced oral bioavailability of poorly water soluble drugs. *Molecules*. 2019;24(19):1–21. https://doi.org/10.3390/molecules24193471.
- Mackaplow MB, Zarraga IE, Morris JF. Rotary spray congealing of a suspension: effect of disk speed and dispersed particle properties. J Microencapsul. 2006;23 (7):793–809. https://doi.org/10.1080/09687860600945446.
- Akiyama Y, Yoshioka M, Horibe H, Hirai S, Kitamori N, Toguchi H. Novel oral controlled-release microspheres using polyglycerol esters of fatty acids. *J Control Release*. 1993;26(1):1–10.
- McGinty S, King D, Pontrelli G. Mathematical modelling of variable porosity coatings for controlled drug release. *Med Eng Phys.* 2017;45:51–60. https://doi.org/10.1016/j.medengphy.2017.04.006.
- Cape JL, Pluntze AM, Nelson ML, et al. Mechanisms of water permeation and diffusive API release from stearyl alcohol and glyceryl behenate modified release

- matrices. *Int J Pharm.* 2020;589(August): 119819. https://doi.org/10.1016/j.iipharm.2020.119819.
- 15. Higuchi T. Mechanism of sustained-action medication. Theoretical analysis of rate of release of solid drugs dispersed in solid matrices. *J Pharm Sci.* 1963;52 (12):1145–1149. https://doi.org/10.1002/jps.2600521210.
- De Coninck E, Vanhoorne V, Boone M, et al. Prilling of API/fatty acid suspensions: screening of additives for drug release modification. *Int J Pharm.* 2020;576(January): 119022. https://doi.org/10.1016/j.ijpharm.2020.119022.
- Wolska E, Sznitowska M, Krzemińska K, Monteiro MF. Analytical techniques for the assessment of drug-lipid interactions and the active substance distribution in liquid dispersions of solid lipid microparticles (SLM) produced de novo and reconstituted from spray-dried powders. *Pharmaceutics*. 2020;12(7):1–23. https://doi.org/ 10.3390/pharmaceutics12070664.
- Baird JA, Taylor LS. Evaluation of amorphous solid dispersion properties using thermal analysis techniques. Adv Drug Deliv Rev. 2012;64(5):396–421. https://doi.org/10.1016/j.addr.2011.07.009.
- Puthli S, Vavia PR. Stability studies of microparticulate system with piroxicam as model drug. AAPS PharmSciTech. 2009;10(3):872–880. https://doi.org/10.1208/ s12249-009-9280-8.
- Markl D, Strobel A, Schlossnikl R, et al. Characterisation of pore structures of pharmaceutical tablets: a review. *Int J Pharm.* 2018;538(1-2):188–214. https://doi.org/10.1016/j.ijpharm.2018.01.017.
- Ewing AV, Kazarian SG. Recent advances in the applications of vibrational spectroscopic imaging and mapping to pharmaceutical formulations. Spectrochim Acta - Part A Mol Biomol Spectrosc. 2018;197:10–29. https://doi.org/10.1016/j.saa.2017.12.055.
- Jiang C, Kuang L, Merkel MP, et al. Biodegradable polymeric microsphere-based drug delivery for inductive browning of fat. Front Endocrinol. 2015;6(NOV):1–11. https://doi.org/10.3389/fendo.2015.00169.
- Qi F, Wu J, Yang T, Ma G, Su Z. Mechanistic studies for monodisperse exenatideloaded PLGA microspheres prepared by different methods based on SPG membrane emulsification. *Acta Biomater*. 2014;10(10):4247–4256. https://doi.org/ 10.1016/j.actbio.2014.06.018.
- Bertoni S, Albertini B, Ronowicz-Pilarczyk J, Calonghi N, Passerini N. Solventfree fabrication of biphasic lipid-based microparticles with tunable structure. *Pharmaceutics*. 2022;14(1):1–22. https://doi.org/10.3390/pharmaceutics14010054.
- D'Emanuele A, Gilpin C. Applications of the environmental scanning electron microscope to the analysis of pharmaceutical formulations. *Scanning*. 1996;18 (7):522–527. https://doi.org/10.1002/sca.1996.4950180709.

- Wei Y, Pence IJ, Evans CL. Quantitative analysis of drug tablet aging by fast hyperspectral stimulated Raman scattering microscopy. 2023;NTu2C.5. doi:10.1364/ ntm.2023.ntu2c.5.
- 27. Sarri B, Canonge R, Audier X, et al. Discriminating polymorph distributions in pharmaceutical tablets using stimulated Raman scattering microscopy. *J Raman Spectrosc*, 2019;50(12):1896–1904. https://doi.org/10.1002/jrs.5743.
- Slipchenko MN, Chen H, Ely DR, Jung Y, Carvajal MT, Cheng JX. Vibrational imaging
  of tablets by epi-detected stimulated Raman scattering microscopy. *Analyst*.
  2010;135(10):2613–2619. https://doi.org/10.1039/c0an00252f.
- Schindelin J, Arganda-Carreras I, Frise E, et al. Fiji: an open-source platform for biological-image analysis. *Nat Methods*. 2012:(9):676–682. https://doi.org/10.1038/nmeth.2019
- Tsikritsis D, Legge EJ, Belsey NA. Practical considerations for quantitative and reproducible measurements with stimulated Raman scattering microscopy. *Analyst*. 2022;147(21):4642–4656. https://doi.org/10.1039/d2an00817c.
- Cook MT, Abou-Shamat MA, Stair JL, Calvo-Castro J. Raman spectroscopy coupled to computational approaches towards understanding self-assembly in thermoreversible poloxamer gels. J Mol Liq. 2022;351: 118660. https://doi.org/10.1016/j. molliq.2022.118660.
- Taylor AJ, Tsikritsis D, Dexter A, Burton A, Bunch J, Belsey NA. Classification of tablet formulations by desorption electrospray ionisation mass spectrometry and transmission Raman spectroscopy. *J Chemom.* 2022;36(6):1–14. https://doi.org/10.1002/cem.3412.
- 33. Socrates G. Infrared and Raman characteristic group frequencies. *Tables Charts*. 2001. http://doi.wiley.com/10.1002/jrs.1238.
- 34. Iwasaki K, Kaneko A, Tanaka Y, Ishikawa T, Noothalapati H, Yamamoto T. Visualizing wax ester fermentation in single Euglena gracilis cells by Raman microspectroscopy and multivariate curve resolution analysis. *Biotechnol Biofuels*. 2019;12 (1):1–10. https://doi.org/10.1186/s13068-019-1471-2.
- Rowe RC, Sheskey PJ, Quinn ME. Handbook of pharmaceutical excipients.; 2009. doi:10.1016/B978-0-12-820007-0.00032-5.
- 36. Kushwah V, Gomes Lopes D, Saraf I, et al. Phase behavior of drug-lipid-surfactant ternary systems toward understanding the annealing-induced change. *Mol Pharm*. 2022;19(2):532–546. https://doi.org/10.1021/acs.molpharmaceut.1c00651.
- Romanus K, Van Neer W, Marinova E, et al. Brassicaceae seed oil identified as illuminant in Nilotic shells from a first millennium AD Coptic church in Bawit, Egypt. Anal Bioanal Chem. 2008;390(2):783–793. https://doi.org/10.1007/s00216-007-1704-2.
- 38. Ferrari AC, Robertson J. Interpretation of Raman spectra of disordered and amorphous carbon. *Phys Rev B*. 2000;61(20):14095–14107.